An Updated Parameterization of Convectively Forced Gravity Wave Drag for Use in Large-Scale Models

HYE-YEONG CHUN

Laboratory for Atmospheric Modeling Research and Department of Atmospheric Sciences, Yonsei University, Seoul, Korea

JONG-JIN BAIK*

Department of Environmental Science and Engineering, Kwangju Institute of Science and Technology, Kwangju, Korea

(Manuscript received 6 October 2000, in final form 30 July 2001)

ABSTRACT

An updated parameterization of gravity wave drag forced by subgrid-scale cumulus convection (GWDC) in large-scale models is proposed. For an analytical formulation of the cloud-top wave stress, two-dimensional, steady-state, linear perturbations induced by diabatic heating are found in a two-layer structure with a piecewise constant shear with a critical level in the lower layer, a uniform flow in the upper layer, and piecewise constant buoyancy frequencies in each layer. The dynamical frame considered is relative to the diabatic forcing and the gravity waves obtained are stationary relative to the diabatic forcing, not necessarily stationary relative to the ground. The cloud-top wave momentum flux is proportional to the square of the magnitude of the convective heating, inversely proportional to the basic-state wind speed, and related to the buoyancy frequencies in each layer. The effect of wind shear in the convective region on the cloud-top momentum flux is negligible, while a difference in the stability between the two layers affects the momentum flux significantly. The cloud-top momentum flux increases as the stability in the convective region decreases and the stability above it increases. A global distribution of the 200-mb wave stress calculated using climatological data reveals that the wave stress in the present study is larger than that in a uniform wind and stability case. This is mainly due to the stability difference between the convective region and the region above it. A methodology of parameterizing GWDC in large-scale models using the wave saturation hypothesis is presented.

1. Introduction

Recently, convectively generated gravity waves and their effects on the large-scale flow have received much attention as an alternative source of gravity wave drag (GWD) in large-scale models. Cumulus clouds impinging on a stably stratified stratosphere can generate gravity waves that influence the large-scale flow through GWD. Convectively generated gravity waves might have a significant direct impact on the Tropics where persistent cumulus clouds exist, and they are considered to be an important source of the quasi-biennial oscillation (QBO) of the tropical stratosphere (Sato and Dunkerton 1997; Alexander and Holton 1997). Convectively generated gravity waves can be equally important in extratropical regions due to the interactions between zonal mean flow, planetary waves, and gravity waves with multiple positive and negative feedbacks, as discussed by Rind et al. (1988b) and Chun et al. (2001).

There have been several attempts to parameterize gravity wave drag induced by subgrid-scale cumulus convection (GWDC) in large-scale models based on different theoretical bases. Rind et al. (1988a) parameterized GWDC on the basis of Lindzen's (1984) formulation, which assumes that the gravity wave momentum flux is proportional to the square of vertically integrated convective mass flux. The resultant cloud-top momentum flux is proportional to the buoyancy frequency at the top of convective region for a given convective mass flux. Kershaw (1995) formulated convectively generated gravity wave momentum flux using a linear, monochromatic gravity wave theory under the assumption that the wave energy above the convective region is proportional to the convective kinetic energy in the cloud region. He showed that the cloud-top wave stress is proportional to the basic-state wind speed relative to a moving convective system and inversely proportional to the buoyancy frequency for a given convective kinetic energy. With a cloud-resolving model, the parameterization was validated and an efficiency factor of con-

* Current affiliation: School of Earth and Environmental Sciences, Seoul National University, Seoul, Korea.

Corresponding author address: Prof. Hye-Yeong Chun, Department of Atmospheric Sciences, Yonsei University, Seoul 120-749, Korea.
E-mail: chy@atmos.yonsei.ac.kr

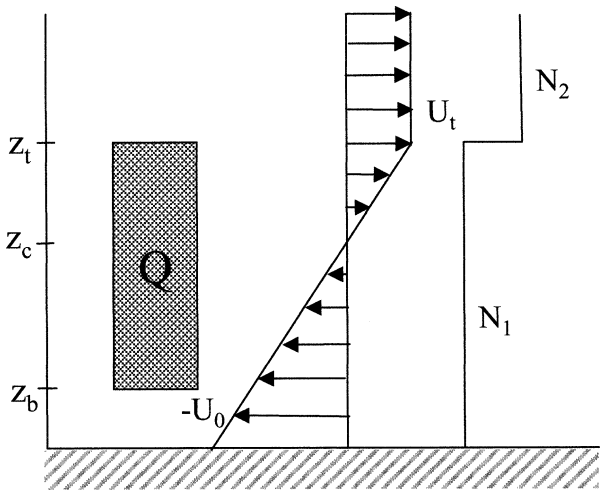

FIG. 1. The structure of the basic-state wind and stability used in this study. The symbols z_b, z_t, and z_c represent the bottom and top heights of the diabatic forcing and the critical level height, respectively. U_0 and U_t are the magnitudes of the basic-state wind at the surface and forcing top, respectively, and N_1 and N_2 are the buoyancy frequencies in regions 1 and 2, respectively.

verting the convective kinetic energy to the wave energy was estimated. This efficiency factor was demonstrated to be rather sensitive to model resolution and the types of convective systems simulated.

Unlike the two studies mentioned above, which employ a monochromatic wave theory, Chun and Baik (1998, CB98 hereafter) derived an analytical expression of the gravity wave momentum flux forced by specified diabatic forcing representing the latent heating of cumulus convection in uniform basic-state wind and buoyancy frequency. They showed that the formulation of the cloud-top wave stress is analogous to that of mountain drag (Pierrehumbert 1986) if the nondimensional mountain height (Nh/U, where N is the buoyancy frequency, h the mountain height, and U the basic-state wind speed) is replaced by the nonlinearity factor of thermally induced internal gravity waves proposed by Lin and Chun (1991). The cloud-top wave stress was shown to be inversely proportional to the basic-state wind speed and the cube of the buoyancy frequency for a given diabatic heating rate. Based on the analytical formulation of the cloud-top wave stress, they proposed a parameterization scheme using the wave saturation hypothesis of Lindzen (1981).

The formulations of the cloud-top wave stress, most important for GWDC parameterization, are different in each of the three studies (Rind et al. 1988a; Kershaw 1995; CB98). Most importantly, the dependency of the cloud-top wave stress on the basic-state wind speed and stability differs from each other. It is, however, not straightforward to compare this dependency (especially in the first two studies) due to implicitly coupled parameters. For example, the convective kinetic energy in Kershaw's formulation and the vertically integrated mass flux in that of Rind et al. are strongly coupled to the basic-state wind shear. In this sense, a direct comparison of the dependency on the basic-state variables in these two formulations (Kershaw 1995) may not be appropriate.

The discrepancy of the dependency of the cloud-top wave stress on the basic-state variables in the three studies stimulates a further investigation of the cloud-top wave stress in realistic atmospheric flow condition. In this study, we reformulate the cloud-top wave stress of CB98 by including a realistic basic-state flow structure having vertical wind shear with a critical level in the convective region and constant buoyancy frequencies in the convective region and above it. The dynamical frame considered in this study is relative to the diabatic forcing, whether it is stationary or moving with respect to the ground, and the critical level is the level at which the basic-state wind (relative to the ground) is the same as the propagation speed of the diabatic forcing. That is, gravity waves considered are stationary waves relative to the diabatic forcing, not necessarily stationary waves relative to the ground. Also, an updated parameterization scheme is proposed in accordance with a change in the basic-state structure. In section 2, analytical solutions of thermally induced internal gravity waves and horizontally integrated wave momentum flux are obtained. Then, the effects of wind shear and stability difference on the wave amplitude and momentum flux above the convective region are presented. In section 3, a methodology of parameterizing GWDC for use in large-scale models is presented. Also, it includes a comparison between the cloud-top wave stresses that are calculated using present and CB98 expressions with the National Centers for Environmental Prediction–National Center for Atmospheric Research (NCEP–NCAR) reanalysis data. In section 4, a summary and conclusions are given.

2. Theory

a. Governing equations and solutions

Consider a two-dimensional, steady-state, nonrotating, hydrostatic, inviscid, Boussinesq airflow system. The governing equations for small amplitude perturbations can be written as

$$U\frac{\partial u}{\partial x} + \frac{dU}{dz}w + \frac{\partial \phi}{\partial x} = 0, \tag{1}$$

$$\frac{\partial \phi}{\partial z} = b, \tag{2}$$

$$U\frac{\partial b}{\partial x} + N^2 w = \frac{gQ}{c_p T_0}, \tag{3}$$

$$\frac{\partial u}{\partial x} + \frac{\partial w}{\partial z} = 0. \tag{4}$$

Here, u and w are the perturbation velocities in the x

and z directions, respectively, ϕ the perturbation kinematic pressure, b the perturbation buoyancy, g the gravitational acceleration, Q the diabatic forcing, c_p the specific heat at constant pressure, and T_0 the reference temperature.

Equations (1)–(4) can be combined into a single equation for the perturbation vertical velocity, which, after taking the Fourier transform in x ($\rightarrow k$), becomes

$$\frac{\partial^2 \hat{w}}{\partial z^2} + \left(\frac{N^2}{U^2} - \frac{U_{zz}}{U}\right)\hat{w} = \frac{g\hat{Q}}{c_p T_0 U^2}, \tag{5}$$

where U_{zz} is a second derivative of U with respect to z. Following CB98, the diabatic forcing Q is specified as

$$Q(x, z) = \begin{cases} Q_0\left(\dfrac{a_1^2}{x^2 + a_1^2} - \dfrac{a_1 a_2}{x^2 + a_2^2}\right) & \text{for } z_b \le z \le z_t, \\ 0 & \text{for elsewhere.} \end{cases} \tag{6}$$

Here, Q_0 is the magnitude of the diabatic forcing, a_1 is the half-width of the forcing, z_b and z_t are the bottom and top heights of the forcing, respectively. The second term with a_2 ($>a_1$) in (6) is introduced to avoid a net forcing problem in a steady-state, nonrotating, inviscid flow system (Smith and Lin 1982). In this study, we consider a two-layer atmosphere (Fig. 1). The basic-state wind has a constant shear in region 1 from the surface to the forcing top (z_t) with a critical level (z_c) somewhere in the region, and is constant above the forcing top (region 2). The buoyancy frequency is assumed to be piecewise constant in each region:

$$U(z) = \begin{cases} -U_0 + \alpha z, & N(z) = N_1, \quad \text{for } 0 \le z \le z_t, \\ U_t, & N(z) = N_2, \quad \text{for } z > z_t, \end{cases} \tag{7}$$

where U_0 is the basic-state wind speed at the surface, α the vertical wind shear (U_0/z_c), and U_t the basic-state wind speed at $z = z_t$.

The general solution of (5) can be written as

$$\hat{w}_1(k, z) = A_1(k)(z - z_c)^{1/2+i\mu} + B_1(k)(z - z_c)^{1/2-i\mu} \quad \text{for } 0 \le z < z_b, \tag{8a}$$

$$\hat{w}_1(k, z) = A_2(k)(z - z_c)^{1/2+i\mu} + B_2(k)(z - z_c)^{1/2-i\mu} + \frac{g\hat{Q}}{c_p T_0 N_1^2} \quad \text{for } z_b \le z \le z_t, \tag{8b}$$

$$\hat{w}_2(k, z) = A_3(k)e^{i\lambda(z-z_t)} + B_3(k)e^{-i\lambda(z-z_t)} \quad \text{for } z > z_t. \tag{8c}$$

Here, $\mu = (\mathrm{Ri} - 1/4)^{1/2}$, where Ri is the Richardson number defined by $\mathrm{Ri} = N_1^2/\alpha^2$ and $\lambda = N_2/U_t$. Although this study is concerned with a dynamically stable case ($\mathrm{Ri} > 1/4$), the above solution is also valid for $\mathrm{Ri} < 1/4$. There exists a branch point at $z = z_c$. We pick the branch $z - z_c = |z - z_c|$ for $z > z_c$ and $z - z_c = |z - z_c|e^{-i\pi}$ for $z < z_c$ from causality (Booker and Bretherton 1967). The six unknowns $A_1(k)$, $B_1(k)$, $A_2(k)$, $B_2(k)$, $A_3(k)$, and $B_3(k)$ can be determined by six boundary and interface conditions. The flat bottom boundary condition requires $\hat{w} = 0$ at $z = 0$. The upper radiation boundary condition allowing for upward energy propagation requires $B_3(k) = 0$ for $U_t > 0$. The interface conditions at $z = z_b$ appear to indicate that both $\hat{w}$ and $\partial\hat{w}/\partial z$ are continuous across the interface. At the interface of different regions ($z = z_t$), the continuity of the vertical velocity ($\hat{w}_1 = \hat{w}_2$) and pressure [$\partial\hat{w}_2/\partial z = \partial\hat{w}_1/\partial z - \hat{w}_1/(z_1 - z_c)$] is imposed. Applying these conditions to (8) determines the six unknowns (appendix). After taking the inverse Fourier transform in k ($\rightarrow x$), the perturbation vertical velocity in the physical space can be obtained:

$$w_1(x, z) = \frac{gQ_0}{c_p T_0 N_1^2}\mathrm{Re}\{A_1(k)[(z - z_c)^{1/2+i\mu} - (-z_c)^{2i\mu}(z - z_c)^{1/2-i\mu}](\mathrm{FR} + i\mathrm{FI})\} \quad \text{for } 0 \le z < z_b, \tag{9a}$$

$$w_1(x, z) = \frac{gQ_0}{c_p T_0 N_1^2}\mathrm{Re}\{A_2(k)[(z - z_c)^{1/2+i\mu} + B_2(k)(z - z_c)^{1/2-i\mu} + 1](\mathrm{FR} + i\mathrm{FI})\} \quad \text{for } z_b \le z \le z_t, \tag{9b}$$

$$w_2(x, z) = \frac{gQ_0}{c_p T_0 N_1^2}\mathrm{Re}\{A_3(k)e^{i\lambda(z-z_t)}(\mathrm{FR} + i\mathrm{FI})\} \quad \text{for } z > z_t, \tag{9c}$$

where

$$\mathrm{FR} = \frac{a_1^2}{x^2 + a_1^2} - \frac{a_1 a_2}{x^2 + a_2^2}, \qquad \mathrm{FI} = \frac{a_1 x}{x^2 + a_1^2} - \frac{a_1 x}{x^2 + a_2^2}.$$

In (9), Re{ } means a real part of { }. From the mass continuity equation (4), the perturbation horizontal velocity can be given by

$$u_1(x, z) = \frac{gQ_0}{c_p T_0 N_1^2}\mathrm{Re}\{A_1(k)[(1/2 + i\mu)(z - z_c)^{-1/2+i\mu} - (-z_c)^{2i\mu}(1/2 - i\mu)(z - z_c)^{-1/2-i\mu}]i(\mathrm{FRI} + i\mathrm{FII})\}$$

$$\text{for } 0 \le z < z_b, \tag{10a}$$

$$u_1(x, z) = \frac{gQ_0}{c_p T_0 N_1^2}\mathrm{Re}\{[A_2(k)(1/2 + i\mu)(z - z_c)^{-1/2+i\mu} + B_2(k)(1/2 - i\mu)(z - z_c)^{-1/2-i\mu}]i(\mathrm{FRI} + i\mathrm{FII})\}$$

$$\text{for } z_b \le z \le z_t, \tag{10b}$$

$$u_2(x, z) = -\frac{gQ_0\lambda}{c_p T_0 N_1^2}\mathrm{Re}\{A_3(k)e^{i\lambda(z-z_t)}(\mathrm{FRI} + i\mathrm{FII})\} \quad \text{for } z > z_t, \tag{10c}$$

where

$$\mathrm{FRI} = \frac{1}{2}a_1 \ln\left(\frac{x^2 + a_2^2}{x^2 + a_1^2}\right),$$

$$\mathrm{FII} = a_1\left[\tan^{-1}\left(\frac{x}{a_1}\right) - \tan^{-1}\left(\frac{x}{a_2}\right)\right].$$

The above analytical solutions of the perturbation vertical and horizontal velocities indicate that the vertical structure of thermally induced internal gravity waves is determined by the Richardson number and the vertical wavelength of dominant gravity waves in region 2 ($\lambda_z = 2\pi/\lambda$) for given heights of forcing top and bottom and a given critical level. The effects of the Richardson number on the steady response of a stably stratified shear flow with a critical level to thermal forcing were investigated by Lin (1987) and Chun et al. (1999). Figure 2 shows the perturbation vertical velocity field. The parameters specified are $z_1 = 1.5$ km, $z_t = 11$ km, $z_c = 5$ km, $N_1 = 0.01$ s^{-1}, $N_2 = 0.02$ s^{-1}, $U_t = 20$ m s^{-1}, $Q_0 = 1$ J kg^{-1} s^{-1}, $a_1 = 10$ km, $a_2 = 5\ a_1$, and $T_0 = 273$ K. The computed U_0, α, and Ri are 16.7 m s^{-1}, 0.0033 s^{-1}, and 9, respectively. This figure exhibits that the steady response of an atmosphere to diabatic heating across a critical level is upward motion in the forcing region and vertically propagating gravity waves above it. There exist two vertical velocity maximums below and above the critical level. This suggests that the response of an atmosphere to diabatic forcing across a critical level can be considered as a sum of the response to diabatic forcing from the forcing bottom to the critical level and that from the critical level to the forcing top, as clearly shown by Baik et al. (1999).

Figure 3 shows the domain-maximum perturbation vertical velocity as a function of the basic-state wind speed at the heating-top height (from $U_t = 6$ m s^{-1} to 40 m s^{-1}) with a critical level height of 5 km. Since the cloud top is located at $z = 11$ km, the magnitude of U_t represents the basic-state wind shear between 6

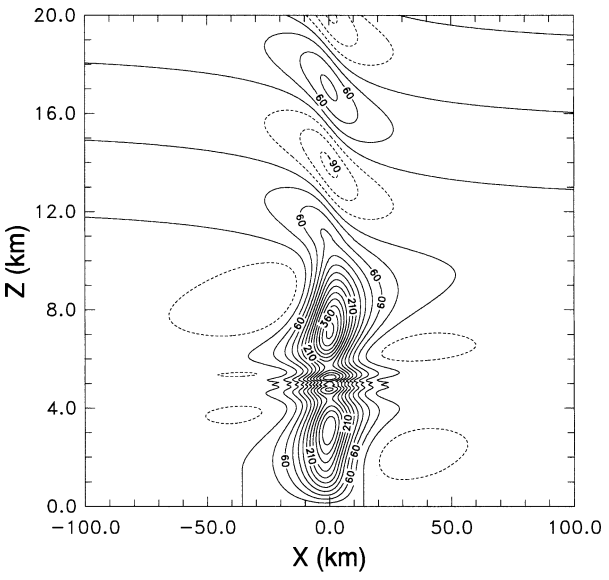

FIG. 2. Perturbation vertical velocity field by (9). The parameters used are $z_1 = 1.5$ km, $z_t = 11$ km, $z_c = 5$ km, $N_1 = 0.01$ s^{-1}, $N_2 = 0.02$ s^{-1}, $U_t = 20$ m s^{-1}, $Q_0 = 1$ J kg^{-1} s^{-1}, $a_1 = 10$ km, $a_2 = 5\ a_1$, and $T_0 = 273$ K. The Richardson number associated with the basic flow is 9. The contour interval is 0.03 m s^{-1}.

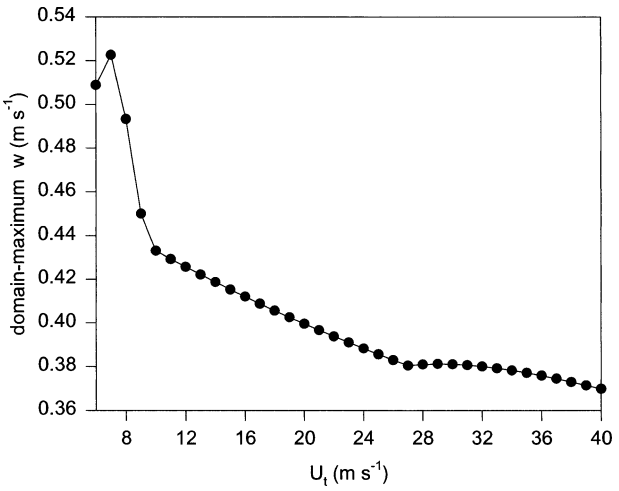

FIG. 3. The domain-maximum perturbation vertical velocity as a function of the basic-state wind speed at the heating-top height. The critical level is fixed at $z = 5$ km. The parameters considered are the same as in Fig. 2.

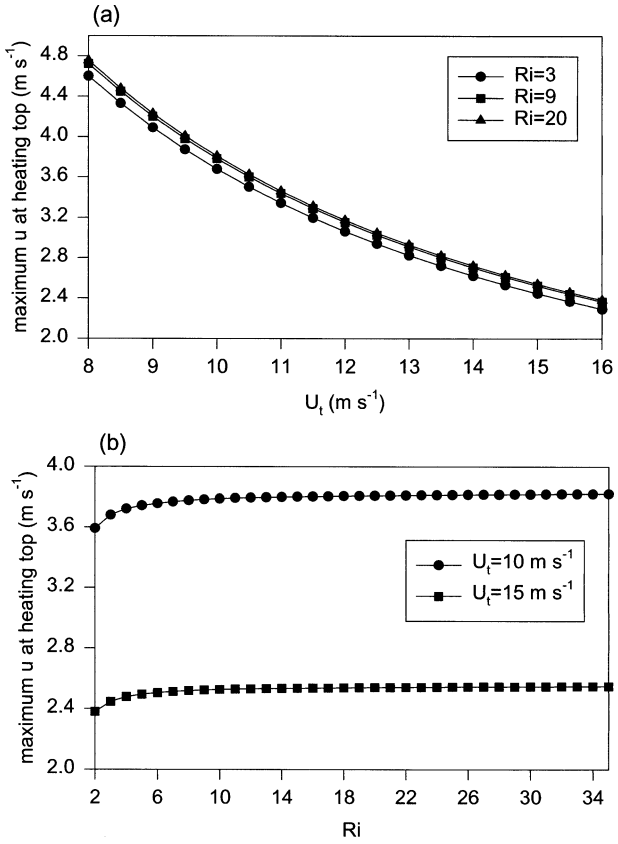

FIG. 4. The maximum perturbation horizontal velocity at the heating-top height (a) as a function of the basic-state wind speed at the heating-top height (U_t) for fixed Richardson numbers and (b) as a function of the Richardson number for fixed U_t.

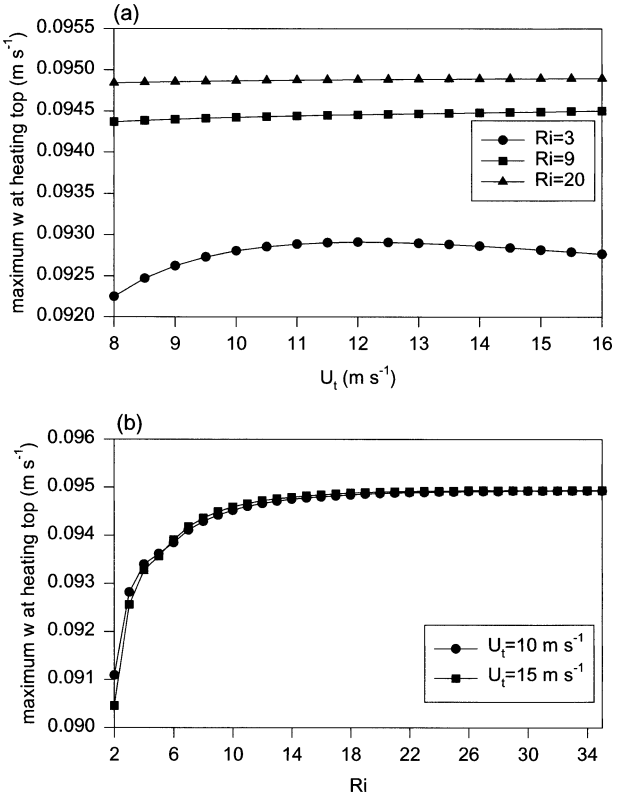

FIG. 5. The same as Fig. 4 except for the perturbation vertical velocity.

km. The corresponding Richardson number ranges from 100 to 2.2 using $N_1 = 0.01$ s^{-1}. The other parameters are the same as in Fig. 2. Because the basic-state wind shear is proportional to U_t for a fixed critical level, Fig. 3 illustrates the effects of both the basic-state wind shear in the forcing region in terms of the Richardson number and the magnitude of U_t. The domain-maximum vertical velocity decreases with increasing wind shear for a wide range of the Richardson numbers. The inverse relationship between the basic-state wind shear and the domain-maximum vertical velocity has been previously noted in several theoretical studies (Lin and Chun 1991; Chun 1997; Chun et al. 1999) and in a numerical modeling study of Kershaw (1995).

Equation (10c) indicates that the magnitude of the perturbation horizontal velocity above the forcing region is proportional to λ. That is, it is inversely proportional to U_t for given Richardson number and stability. However, because the coefficient $A_3(k)$ in (8c) contains a Richardson-number dependency (see appendix), a combination of Ri and U_t determines the magnitude of the perturbation horizontal velocity above the forcing region. To separate the individual effect of wind shear and U_t on the cloud-top gravity waves, two calculations are carried out: one by changing the Richardson number with a fixed U_t and the other by changing U_t with a fixed value of Ri. In both cases, the critical level varies according to a change in Ri or U_t.

The calculated results are plotted in Fig. 4. The ranges of U_t and Ri in Fig. 4 are chosen so as to satisfy (i) linearity (perturbation horizontal velocity cannot be comparable to U_t), (ii) $U_0 > 0$, and (iii) $z_b < z_c < z_t$. The maximum perturbation horizontal velocity decreases monotonically with increasing U_t for a given Richardson number and increases with decreasing shear (high Ri) for a given U_t (Fig. 4a). Except for low Richardson-number flows (Ri < 5), the maximum perturbation horizontal velocity is independent of Ri but inversely proportional to U_t (Fig. 4b). From Fig. 4, it can be concluded that the cloud-top perturbation horizontal velocity is inversely proportional to the basic-state wind speed there without any strong dependency on wind shear in the convective region.

The situation is different for the perturbation vertical velocity at the heating-top height (Fig. 5). Except for the low Richardson-number flow (Ri = 3), the maximum vertical velocity remains almost constant with U_t for a fixed Ri and increases with increasing Richardson number (Fig. 5a). However, the Richardson-number dependency of the heating-top vertical velocity is limited to low Richardson-number flows (Fig. 5b). The maxi-

mum vertical velocity at the heating-top height is very small overall and its difference with U_t (less than 10^{-3} m s^{-1}) is one order of magnitude smaller than that with Ri (less than 10^{-2} m s^{-1}). Figure 5 suggests that the magnitude of the perturbation vertical velocity at the cloud top increases as the wind shear in the convective region decreases, exclusively for strong shear flows.

b. Momentum flux

The vertical flux of the integrated horizontal momentum M is defined by

$$M = \rho_0 \int_{-\infty}^{\infty} uw\, dx, \tag{11}$$

where ρ_0 is the basic-state density. From the perturbation horizontal and vertical velocities given by (10) and (9), the momentum flux can be obtained analytically. Even though the analytical expression of the momentum flux can be found from the surface to the above forcing region, only the momentum flux above the forcing region is needed for current GWDC parameterization. The reason for this is that the momentum flux in the forcing region is generated mainly by the forcing representing cumulus clouds with turbulent characteristics, rather than by gravity waves. The momentum flux at the cloud top, which can be used for a reference-level wave stress for GWDC parameterization, is

$$M_{ct} = -\rho_0 \pi a_1^2 \left(\frac{gQ_0}{c_p T_0 N_1^2}\right)^2 \mathrm{Sgn}(U_t) \frac{N_2}{|U_t|} |A|^2 \times \ln\left[\frac{(a_1 + a_2)^2}{4a_1 a_2}\right], \tag{12}$$

where

$$A = \frac{A_3}{F} = \left[\frac{(1/2 - i\mu)X_{12}X_8 - (1/2 + i\mu)X_7 + (z_t - z_c)(z_b - z_c)^{-1}X_4}{Y_2 - X_{12}Y_3}\right].$$

Using the expressions given in the appendix, $|A|^2$ is given by

$$|A|^2 = \frac{|A_2|^2}{|A_1|^2}, \tag{13}$$

where

$$\begin{aligned}
|A_1|^2 &= e^{4\pi\mu}\{1/4 + [\lambda(z_t - z_c) + \mu]^2\} \\
&\quad - 2e^{2\pi\mu}\{[1/4 + \lambda^2(z_t - z_c)^2 - \mu^2]\cos\theta_1 \\
&\qquad - \mu \sin\theta_1\} + 1/4 + [\lambda(z_t - z_c) - \mu]^2, \\
|A_2|^2 &= e^{4\pi\mu}(1/4 + \mu^2) \\
&\quad - 2e^{3\pi\mu}\sqrt{z_1}[\mu\cos\theta_2 + (\mu^2 - 1/4)\sin\theta_2 \\
&\qquad - (1/4 + \mu^2)\sin\theta_3] \\
&\quad + 2e^{2\pi\mu}\{z_1[1/4 + \mu^2/2 + (\mu^2 - 1/4)\cos\theta_4 \\
&\qquad - \mu\sin\theta_4] \\
&\qquad + [(\mu^2 - 1/4)\cos\theta_1 - \mu\sin\theta_1]\} \\
&\quad - 2e^{\pi\mu}\sqrt{z_1}[(\mu^2 + 1/4)\sin\theta_3 \\
&\qquad - (\mu^2 - 1/4)\sin\theta_2 - \mu\cos\theta_2] \\
&\quad + 1/4 + \mu^2,
\end{aligned}$$

where

$$z_1 = \frac{z_t - z_c}{z_c - z_b}, \qquad \theta_1 = 2\mu \ln\left(\frac{z_c}{z_t - z_c}\right),$$

$$\theta_2 = \mu \ln\left[\frac{z_c^2}{(z_t - z_c)(z_c - z_b)}\right], \qquad \theta_3 = \mu \ln\left(\frac{z_t - z_c}{z_c - z_b}\right),$$

$$\theta_4 = 2\mu \ln\left(\frac{z_c}{z_c - z_b}\right).$$

Because the terms including $e^{4\pi\mu}$ dominate other terms in (13), $|A|^2$ can be approximated by

$$|A|^2 = \left(1 + 2\sqrt{\frac{\mathrm{Ri} - 1/4}{\mathrm{Ri}}}N_{12} + N_{12}^2\right)^{-1}, \tag{14}$$

where $N_{12} = N_2/N_1$. For $\mathrm{Ri} \gg 1$, (14) can be further approximated by

$$|A|^2 = \left(\frac{N_{21}}{1 + N_{21}}\right)^2, \tag{15}$$

where $N_{21} = N_1/N_2$. The difference between (13) and (14) becomes smaller for higher Richardson-number flow because the terms including $e^{4\pi\mu}$ increase exponentially with Ri. The approximation (15) from (14) becomes much more accurate for higher Richardson-number flow. However, even for the small Richardson-number flow (Ri = 3), the difference between (13) and (14) [(14) and (15)] is less than 10^{-4} [10^{-3}] for $0.5 \leq N_{21} \leq 1.0$. Figure 6 shows the calculated $|A|^2$ using (14) for Ri = 3, 7, and 16 and (15) as a function of N_{21}. Here $|A|^2$ increases with N_{21} for a given Ri and

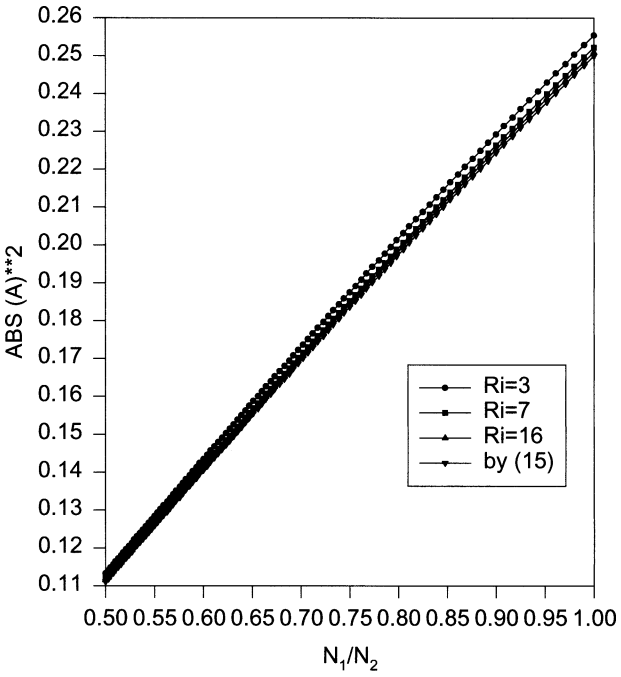

FIG. 6. The quantity $|A|^2$ calculated using (14) for selected Richardson numbers (Ri = 3, 7, 16) and (15) as a function of N_{21} ($=N_1/N_2$).

does not depend strongly on Ri when it is larger than 7. For a given Ri, the approximation (15) is more accurate when the buoyancy frequency above the convective region is larger than that in the convective region.

Then, the momentum flux at the cloud top is expressed by

$$M_{\rm ct} = -\rho_0 \pi a_1^2 \left(\frac{gQ_0}{c_p T_0 N_1^2}\right)^2 \mathrm{Sgn}(U_t) \frac{N_2}{|U_t|} \left(\frac{N_{21}}{1 + N_{21}}\right)^2 \times \ln\left[\frac{(a_1 + a_2)^2}{4a_1 a_2}\right]. \quad (16)$$

This formulation indicates that the magnitude of the cloud-top momentum flux is proportional to the square of the magnitude of the diabatic heating, inversely proportional to the cloud-top basic-state wind speed, and related to the buoyancy frequencies in the convective region and above it. Compared with the momentum flux of CB98 in constant basic-state wind and stability, which is given by

$$M_{\rm ct} = -\rho_0 \pi a_1^2 \left(\frac{gQ_0}{c_p T_0 N^2}\right)^2 \mathrm{Sgn}(U) \frac{N}{|U|} \times (\cos\lambda z_t - \cos\lambda z_b)^2 \ln\left[\frac{(a_1 + a_2)^2}{4a_1 a_2}\right], \quad (17)$$

a few points are noteworthy. First, the basic-state wind shear in the convective region does not explicitly influence the cloud-top momentum flux. This is because the Richardson-number dependency is negligible in (15). Even though U_t can be associated with a shear between the critical level and the cloud top, it cannot be a direct representation of wind shear in the convective region unless a critical level is fixed. The Richardson number is a direct measure of wind shear for a fixed N_1.

Second, the cloud-top momentum flux is strongly coupled to the buoyancy frequencies in the convective region and above it for given cloud-top basic-state wind speed and diabatic forcing parameters. From (16), it is distinguished that the buoyancy frequency in the term $(gQ_0/c_pT_0N^2)^2$ in (17) is N_1 rather than N_2. In the CB98 GWDC parameterization, all Ns in (17) are evaluated at the cloud top. The term $(gQ_0/c_pT_0N_1^2)^2$ in (16) is equivalent to the magnitude of w^2 in the convective region from (9). Therefore, if we choose a maximum value of Q_0 in a grid column and a buoyancy frequency where the maximum Q_0 occurs, this term can be regarded as $w_{\rm max}^2$ as defined by Kershaw (1995). To examine the overall dependency of the momentum flux on N_1 and N_2, the terms $N_2/N_1^4[N_{21}/(1 + N_{21})]^2$ (Fig. 7a) and $N_2[N_{21}/(1 + N_{21})]^2$ (Fig. 7b) in (16) are calculated in a range of N_1 and N_2 from 0.006 s^{-1} to 0.022 s^{-1}. The term $N_2[N_{21}/(1 + N_{21})]^2$ is plotted to get some insight of the dependency of the momentum flux on stability in the case where $w_{\rm max}^2$ is known. Figure 7a shows that the magnitude of the momentum flux strongly depends on (inversely proportional to) N_1, as expected by a factor of $1/N_1^4$. However, the situation is different in the field of $N_2[N_{21}/(1 + N_{21})]^2$, which shows (Fig. 7b) that the magnitude of the momentum flux is almost linearly proportional to N_1. The dependency of the momentum flux on N_1 when $w_{\rm max}^2$ is known does not appear in Kershaw (1995). For a fixed N_1, either $N_2/N_1^4[N_{21}/(1 + N_{21})]^2$ or $N_2[N_{21}/(1 + N_{21})]^2$ is inversely proportional to N_2 for $N_2 > N_1$.

The magnitude of the momentum flux near $z = 15$ km ($\rho_0 \sim 0.2$ kg m^{-3}) calculated using (16) is about 0.5×10^3 N m^{-1} with the parameters used in Fig. 2. If the momentum flux is horizontally averaged over ~10 km, the value at the cloud top is about -0.05 N m^{-2}. This value is close to the momentum flux numerically obtained by Kershaw (1995) (-0.043 N m^{-2}) in an experiment with the same wind shear of (20 m s^{-1})/(6 km). However, since he calculated the momentum flux at $z = 8$ km (cloud-top height in his case is 6 km), the estimated momentum flux near $z = 15$ km can be -0.107 N m^{-2} considering the density difference ($\rho_0 \sim 0.5$ kg m^{-3} near $z = 8$ km). It can be expected that the magnitude of the momentum flux in the present study is smaller than that in the cloud-model simulations. In the linear study, the parameters are chosen so as to satisfy the condition that the perturbation horizontal velocity is small enough compared with the basic-state wind speed. The magnitude of the averaged momentum flux calculated using (17) is at least one order magnitude smaller than that obtained by (16) if $N =$

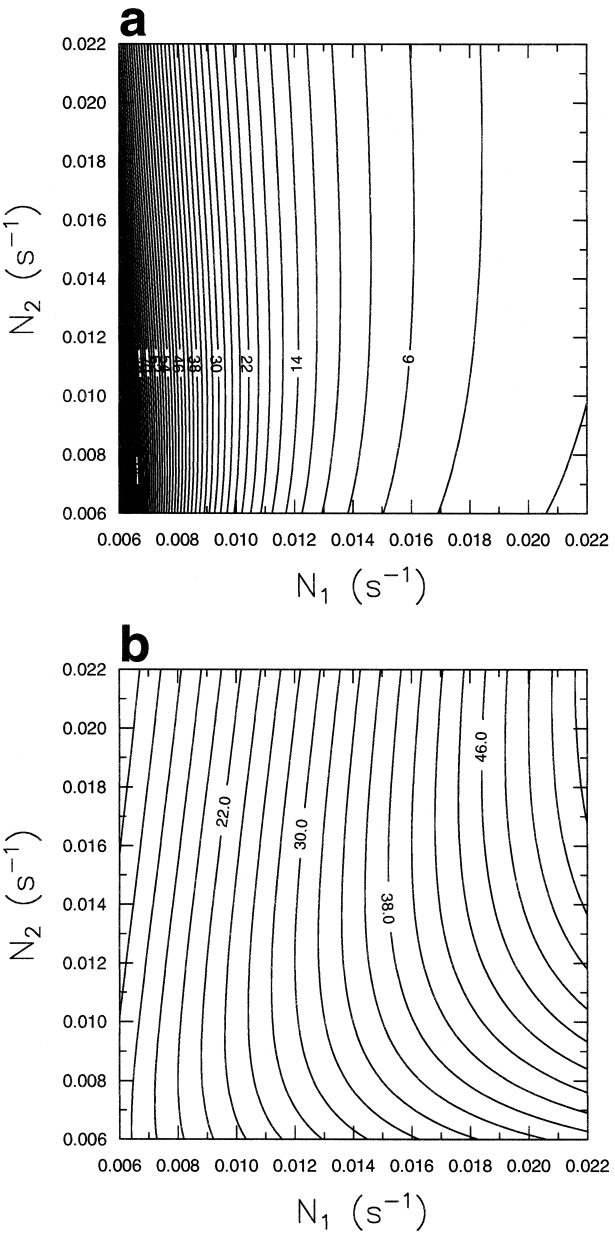

FIG. 7. The fields of (a) $N_2/N_1^4[N_{21}/(1 + N_{21})]^2$ and (b) $N_2[N_{21}/(1 + N_{21})]^2$ in a range of N_1 and N_2 from 0.006 s^{-1} to 0.022 s^{-1}. For better presentation of figures, factors of 10^{-4} and 10^4 are multiplied to (a) and (b), respectively. The contour intervals of (a) and (b) are 2 s^3 and 2 s^{-1}, respectively.

0.02 s^{-1} is used. As long as $N_2 > N_1$, the momentum flux given by (16) can be larger than that given by (17).

Third, (16) indicates that the momentum flux is inversely proportional to the cloud-top basic-state wind speed. This is also true in CB98. This inverse relationship between the basic-state wind speed (or wind shear) and the momentum flux at the cloud top is a major difference between our study and Kershaw's (1995). In Kershaw's study, the momentum flux was found to be linearly proportional to the basic-state wind speed at the cloud top. This relationship was derived based on the assumption that the vertical displacement above cloud is proportional to the domain-maximum vertical velocity in the convective region. This assumption was presented by the formulation that the vertical displacement is inversely proportional to the buoyancy frequency and proportional to w_{max} in the convective region [Eq. (9) of Kershaw (1995)]. In this study, the vertical displacement above cloud can be analytically obtained by

$$\eta(x, z) = \frac{1}{U_t}\int_{-\infty}^{x} w(x, z)\, dx. \tag{18}$$

Because the magnitude of vertical velocity above cloud is not directly related to the basic-state wind speed there, the vertical displacement is inversely proportional to the basic-state wind speed. This ends up with the momentum flux that is inversely proportional to the basic-state wind speed. The inverse relationship between the wave amplitude and the basic-state wind speed (or wind shear) above cloud is well-represented in the solution of the perturbation horizontal velocity [see (10) and Fig. 4b]. The inverse relationship between the momentum flux and the wind shear is also presented by Chun (1997). Considering that the basic-state wind and stability structure in this study is very similar to that in the numerical simulations of Kershaw, this discrepancy needs to be clarified. This is under investigation with a cloud-resolving model.

3. Parameterization of GWDC for large-scale models

The effects of subgrid-scale gravity wave drag in numerical models can be included in the horizontal momentum equations by

$$\frac{\partial \overline{u}}{\partial t} = -\frac{1}{\rho}\frac{\partial \tau_x}{\partial z}, \tag{19a}$$

$$\frac{\partial \overline{v}}{\partial t} = -\frac{1}{\rho}\frac{\partial \tau_y}{\partial z}, \tag{19b}$$

where $\overline{u}$ and $\overline{v}$ are the zonal and meridional components of wind, respectively, ρ is the air density, and τ_x and τ_y are the zonal and meridional components of the subgrid-scale momentum flux, respectively. The present methodology of parameterizing GWDC for use in large-scale models is the same as in CB98 and Chun et al. (2001), except that some parameters need to be changed according to the updated analytical formulation. A procedure of GWDC parameterization can be summarized as follows:

1) Calculate the wave stress vector at the cloud-top level ($\boldsymbol{\tau}_{ct}$) for each individual cloud or a representative cloud, depending on cumulus parameterization scheme used, in a grid box as

$$\boldsymbol{\tau}_{ct} = -\rho_{ct}\frac{|\mathbf{u}_{ct}|^2}{N_{ct}}\mathbf{u}_{ct}k_s c_1 c_{2ct}^2 \mu_{ct}^2, \tag{20}$$

where

$$c_1 = \pi \ln\left[\frac{(a_1 + a_2)^2}{4a_1 a_2}\right], \qquad c_{2ct} = \frac{N_1/N_{ct}}{1 + N_1/N_{ct}},$$

$$\mu_{ct} = \frac{gQ_0 a_1}{c_p T_0 N_1 |\mathbf{u}_{ct}|^2}\frac{N_{ct}}{N_1}, \qquad k_s = \frac{n}{\Delta x}.$$

The variables with subscript ct are those quantities evaluated at the cloud-top height. Here $\mathbf{u}_{ct}$ is the horizontal wind vector at the cloud top, Δx the grid size in the zonal direction, and n the total number of subensemble clouds in a grid box. Note that in CB98, $n = 1$ is considered. In a numerical model, a maximum diabatic heating rate in a grid column and buoyancy frequency evaluated at the level of the maximum diabatic heating rate can be used for Q_0 and N_1, respectively, as suggested by Chun et al. (2001). The parameter c_1, related to the horizontal structure of the convective forcing, can be evaluated employing $a_2 = 5a_1$, as used in many theoretical studies (Smith and Lin 1982; Lin 1987; Lin and Chun 1991). The a_1 in μ is an approximate horizontal scale of effective cloud and can be approximated following Chun et al. (2001). There exist some uncertainties in determining a_1 in general circulation models where subgrid-scale convective clouds are parameterized. Nevertheless, Chun et al. (2001) showed that using $a_1 = \gamma\Delta x$, where γ is the fractional coverage of clouds within a grid box, and $a_2 = 5a_1$ seems to work reasonably well in the general circulation model in terms of the magnitude of cloud-top wave stress compared with aircraft observations by Pfister et al. (1993).

2) The wave stress τ at any level parallel to the cloud-top stress vector can be written as

$$\tau = \left(\frac{\rho U^3}{N}\right)k_s c_1 c_2^2 \mu^2, \qquad \mu = \frac{gQ_0 a_1}{c_p T_0 N_1 U^2}\frac{N}{N_1}, \tag{21}$$

where

$$c_2 = \frac{N_1/N}{1 + N_1/N},$$

where U is the magnitude of the component of the wind vector $\mathbf{u}$ in the direction of the cloud-top stress vector [$U = (\mathbf{u} \cdot \boldsymbol{\tau}_{ct})/|\boldsymbol{\tau}_{ct}|$]. Unlike CB98, c_2 is not a constant but depends on buoyancy frequency. Also, the nonlinearity factor of thermally induced internal gravity waves μ contains N/N_1 term because μ at any level is equivalent to a ratio of the perturbation horizontal velocity to the basic-state wind speed there. For given forcing parameters, the nonlinearity factor increases with decreasing N_1 and/or increasing N.

3) Define a minimum Richardson number taking into account the wave effect as

$$\mathrm{Ri}_{min} = \frac{\mathrm{Ri}(1 - \mu|c_2|)}{(1 + \mu\mathrm{Ri}^{1/2}|c_2|)^2}, \tag{22}$$

where Ri is the local Richardson number.

4) Check whether wave breaking occurs on the basis of the minimum Richardson number given by (22). That is, if $\mathrm{Ri}_{min} \geq 1/4$, then τ at the level just above the cloud top is set to τ_{ct}. If $\mathrm{Ri}_{min} < 1/4$, then Ri_{min} is set equal to 1/4 following the wave saturation hypothesis of Lindzen (1981) and the saturation stress is calculated using

$$\tau_s = \left[\frac{\rho U^3}{N}\right]k_s c_1 c_2^2 \mu_s^2, \tag{23}$$

$$\mu_s = \frac{1}{|c_2|}\left[2\sqrt{2 + \frac{1}{\sqrt{\mathrm{Ri}}}} - \left(2 + \frac{1}{\sqrt{\mathrm{Ri}}}\right)\right]. \tag{24}$$

5) Repeat the previous steps (2), (3), and (4) at a next higher level unless either τ approaches zero or the model top is reached.

6) Determine the stress components in the zonal and meridional directions by

$$\tau_x = \tau\cos\theta, \qquad \tau_y = \tau\sin\theta, \tag{25}$$

where θ is the angle between the cloud-top stress vector and the zonal direction.

7) Calculate a deposition of the momentum in the cloud region for the momentum conservation by computing the vertically integrated momentum above subensemble clouds or cloud. Following Kershaw (1995), it is assumed that the momentum is deposited only within the layer between the cloud-top level and the level just below it. Then, the acceleration in the cloud region is obtained according to the momentum conservation principle:

$$\int_{\sigma_{ct+1}}^{\sigma_{ct}} \rho\left(\frac{\partial\overline{u}}{\partial t}\right)d\sigma = -\int_{\sigma_{ct}}^{\sigma_1} \rho\left(\frac{\partial\overline{u}}{\partial t}\right)d\sigma, \tag{26a}$$

$$\int_{\sigma_{ct+1}}^{\sigma_{ct}} \rho\left(\frac{\partial\overline{v}}{\partial t}\right)d\sigma = -\int_{\sigma_{ct}}^{\sigma_1} \rho\left(\frac{\partial\overline{v}}{\partial t}\right)d\sigma, \tag{26b}$$

where σ_1, σ_{ct}, and σ_{ct+1} represent the σ levels of the model top and the cloud top, and the σ level just below σ_{ct}, respectively.

A comparison of the cloud-top wave stress of CB98 with that of the present study is made using 19-yr (1979–97) monthly mean NCEP–NCAR reanalysis data (Kalnay et al. 1996) for July. Figure 8 shows the global distributions of the magnitude of the 200-mb wave stress by CB98 (Fig. 8a) and (20) (Fig. 8b). These are calculated using the maximum diabatic heating rate (Q_0/c_p) (Fig. 8c), buoyancy frequency at the level of the maximum convective heating rate (N_1) (Fig. 8d), 200-mb horizontal wind speed (Fig. 8e), and 200-mb buoyancy frequency (N_2) (Fig. 8f). This figure shows that

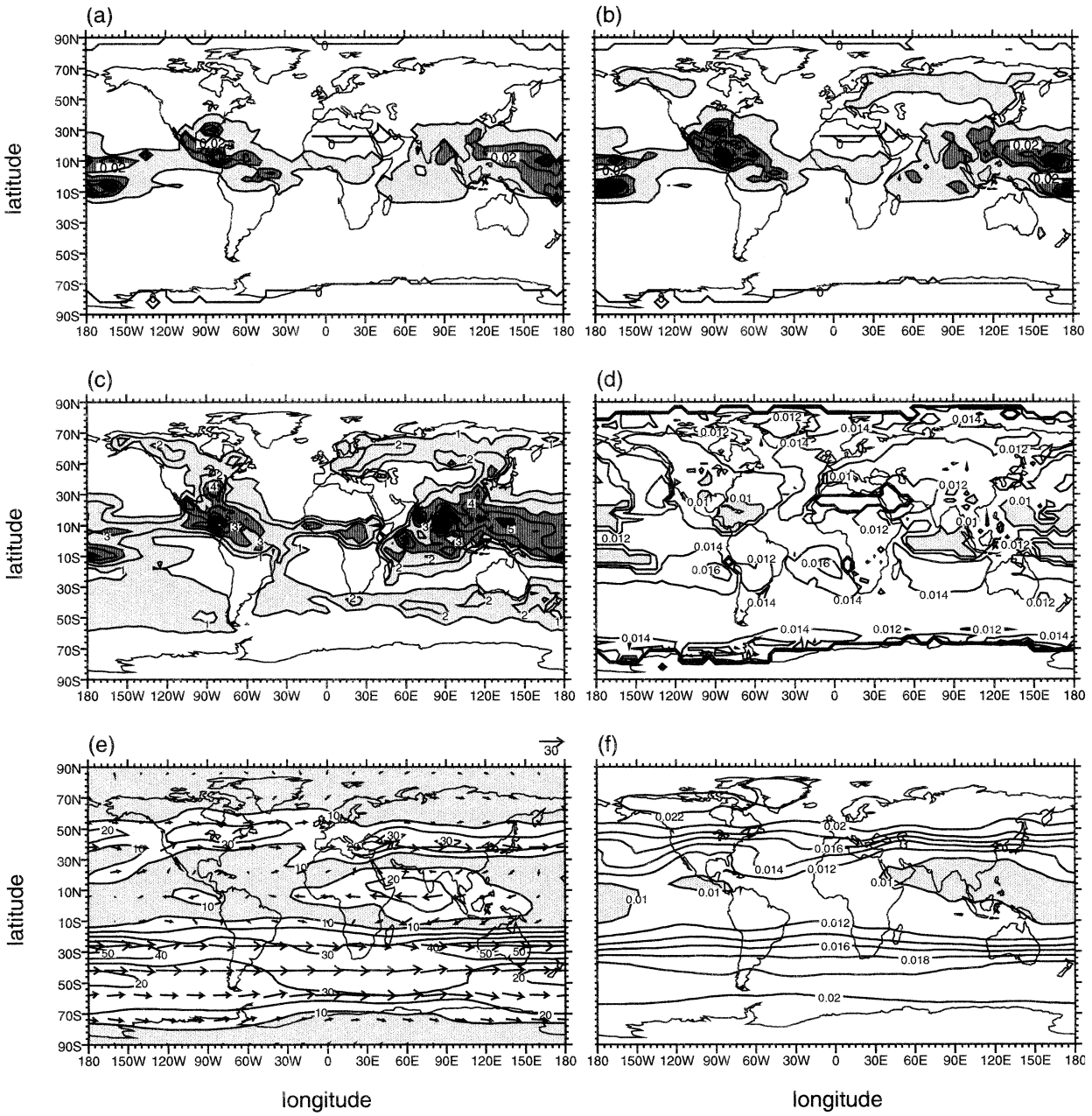

FIG. 8. The global distributions of the magnitude of the cloud-top wave stress at 200 mb based on the formulation of (a) CB98 and (b) present study. These are calculated using the NCEP–NCAR reanalysis data [19-yr (1979–97) averaged Jul mean] of (c) the maximum convective heating rate (Q_0/c_p), (d) the buoyancy frequency at the level of the maximum convective heating rate (N_1), (e) the horizontal wind speed at 200 mb ($|\mathbf{u}_{ct}|$) superimposed on wind vectors, and (f) the buoyancy frequency at 200 mb (N_{ct}). For a direct comparison between CB98 and the present study, $k_s = 1/\Delta x$ and $\Delta x = 5°$ lon are used. The contour intervals of (a)–(f) are 0.02 N m^{-2}, 0.02 N m^{-2}, 1 K day^{-1}, 0.002 s^{-1}, 10 m s^{-1}, and 0.002 s^{-1}, respectively. The light shadings in (a)–(f) denote values less than 0.01 N m^{-2}, 0.01 N m^{-2}, 3 K day^{-1}, 0.01 s^{-1}, 10 m s^{-1}, and 0.01 s^{-1}, respectively.

the magnitude of the 200-mb wave stress in the present study is larger than that by CB98 (maximum values in Figs. 8a and 8b are 0.25 N m^{-2} and 0.41 N m^{-2}, respectively) both in the intertropical convergence zone (ITCZ) and Northern Hemisphere midlatitude. This is mainly because the buoyancy frequency in the convective region is much smaller than that above cloud. The difference in the wave stress between CB98 and the present study becomes larger for higher cloud because the difference between N_1 and N_2 becomes larger. The 100-mb wave stress by the updated formulation (not shown) is generally much larger than that by CB98. Considering that the magnitude of the cloud-top (reference level) wave stress is one of important factors in

estimating the effects of GWDC on the large-scale flow, an increase in the magnitude of the wave stress implies an increase in zonal and meridional wind tendencies due to the GWDC process in large-scale models.

4. Summary and conclusions

The parameterization of gravity wave drag forced by subgrid-scale cumulus convection for use in large-scale models proposed by CB98 has been updated by considering a realistic two-layer atmospheric structure. The basic-state flow structure was assumed to have a constant wind shear with a critical level in the lower layer, a uniform wind above, and piecewise constant buoyancy frequencies in each layer. The thermal forcing representing the latent heating of cumulus convection was specified in the lower layer across a critical level. The solution of thermally induced internal gravity waves was obtained analytically. The dynamical frame considered in this study is relative to the daibatic forcing, whether it is stationary or moving with respect to the ground, and the critical level is the level at which the basic-state wind (relative to the ground) is the same as the propagation speed of the diabatic forcing. That is, gravity waves considered are stationary waves relative to the diabatic forcing, not necessarily stationary waves relative to the ground. It was found that the magnitude of the domain-maximum vertical velocity located in the forcing region is inversely proportional to the wind shear. Above the forcing region, the magnitude of the perturbation horizontal velocity increases mainly with decreasing basic-state wind speed, while the magnitude of the vertical velocity increases mainly with decreasing wind shear (increasing Richardson number) in the convective region.

Using the solutions of the perturbation horizontal and vertical velocities, the horizontally averaged momentum flux at the cloud top was obtained analytically. It was found that the magnitude of the momentum flux is proportional to the square of the diabatic heating rate, inversely proportional to the cloud-top basic-state wind speed, and related to the buoyancy frequencies in each layer. This dependency of the cloud-top wave stress on buoyancy frequency does not appear in a vertically uniform stability case by CB98. Because the buoyancy frequency in the convective region is generally smaller than that above cloud, the magnitude of the cloud-top wave stress in the updated formulation is larger than that of CB98 under the same diabatic heating and wind conditions. The dependency of the cloud-top wave stress on the basic-state wind speed is the same as in CB98 regardless of wind shear. The effect of vertical wind shear in the convective region does not appear in the momentum flux formulation because the wave perturbation at the cloud top is not sensitive to a change in vertical wind shear (or Richardson number) except for relatively low Richardson-number flow (Ri < 3).

A comparison of the cloud-top wave stress of CB98 with that of the present study, using monthly mean climatological data for July, revealed that the magnitude of the 200-mb wave stress in the present study is larger than that of CB98. This is mainly because the buoyancy frequency in the convective region is much smaller than that above cloud. Because the wave stress is one of the most important factors in estimating the effects of GWDC on the large-scale flow, an increase in the wave stress implies an increase in the zonal and meridional wind tendencies owing to the GWDC process in large-scale models. An implementation of the updated GWDC parameterization in an atmospheric general circulation model is under way and better simulated climate is expected.

Acknowledgments. The authors would like to thank two anonymous reviewers for providing many constructive comments that improved the original manuscript. The authors also would like to thank Dr. Peter Roohr of USFK for providing valuable comments on this study. The first author was supported by the Korea Ministry of Science and Technology through the National Research Laboratory Program. Both authors were supported by the Brain Korea 21 Program.

APPENDIX

Six Unknowns in (8)

$$B_2(k) = \frac{-F[X_4Y_2 - X_{12}(X_9 + 1)Y_1]}{Y_1(Y_2 - X_{12}Y_3)},$$

$$A_2(k) = -\frac{1}{X_{12}}\left[B_2(k) + \frac{X_4F}{Y_1}\right],$$

$$A_3(k) = B_2(k)\left(X_8 - \frac{X_7}{X_{12}}\right) + F\left(1 - \frac{X_4X_7}{X_{12}Y_1}\right),$$

$$A_1(k) = \frac{1}{X_3}[A_2(k)X_1 + B_2(k)X_2 + F],$$

$$B_1(k) = -X_{12}A_1(k), \qquad B_3(k) = 0,$$

where

$$X_1 = (z_b - z_c)^{1/2+i\mu}, \qquad X_2 = (z_b - z_c)^{1/2-i\mu},$$

$$X_3 = X_1 - X_{12}X_2,$$

$$X_4 = (1/2 + i\mu)X_1 - X_{12}(1/2 - i\mu)X_2,$$

$$X_5 = (1/2 + i\mu)X_1, \qquad X_6 = (1/2 - i\mu)X_2,$$

$$X_7 = (z_t - z_c)^{1/2+i\mu}, \qquad X_8 = (z_t - z_c)^{1/2-i\mu},$$

$$X_9 = i\lambda(z_t - z_c), \qquad X_{10} = -(1/2 - i\mu)X_7,$$

$$X_{11} = -(1/2 + i\mu)X_8, \qquad X_{12} = (-z_c)^{2i\mu},$$

$$Y_1 = 2i\mu(z_b - z_c), \qquad Y_2 = X_7(X_9 + 1/2 - i\mu),$$

$$Y_3 = X_8(X_9 + 1/2 + i\mu), \qquad F = g\hat{Q}/(c_pT_0N_1^2).$$

REFERENCES

Alexander, M. J., and J. R. Holton, 1997: A model study of zonal forcing in the equatorial stratosphere by convectively induced gravity waves. *J. Atmos. Sci.,* **54,** 408–419.

Baik, J.-J., H.-S. Hwang, and H.-Y. Chun, 1999: Transient, linear dynamics of a stably stratified shear flow with thermal forcing and a critical level. *J. Atmos. Sci.,* **56,** 483–499.

Booker, J. R., and F. R. Bretherton, 1967: The critical layer for internal gravity waves in a shear flow. *J. Fluid Mech.,* **27,** 513–539.

Chun, H.-Y., 1997: Weakly non-linear response of a stably stratified shear flow to thermal forcing. *Tellus,* **49A,** 528–543.

——, and J.-J. Baik, 1998: Momentum flux by thermally induced internal gravity waves and its approximation for large-scale models. *J. Atmos. Sci.,* **55,** 3299–3310.

——, I.-S. Song, and J.-J. Baik, 1999: Some aspects of internal gravity waves in the multicell-type convective system. *Meteor. Atmos. Phys.,* **69,** 205–222.

——, M.-D. Song, J.-W. Kim, and J.-J. Baik, 2001: Effects of gravity wave drag induced by cumulus convection on the atmospheric general circulation. *J. Atmos. Sci.,* **58,** 302–319.

Kalnay, E., and Coauthors, 1996: The NCEP/NCAR 40-Year Reanalysis Project. *Bull. Amer. Meteor. Soc.,* **77,** 437–471.

Kershaw, R., 1995: Parameterization of momentum transport by convectively generated gravity waves. *Quart. J. Roy. Meteor. Soc.,* **121,** 1023–1040.

Lin, Y.-L., 1987: Two-dimensional response of a stably stratified shear flow to diabatic heating. *J. Atmos. Sci.,* **44,** 1375–1393.

——, and H.-Y. Chun, 1991: Effects of diabatic cooling in a shear flow with a critical level. *J. Atmos. Sci.,* **48,** 2476–2491.

Lindzen, R. S., 1981: Turbulence and stress due to gravity wave and tidal breakdown. *J. Geophys. Res.,* **86,** 9707–9714.

——, 1984: Gravity waves in the middle atmosphere. *Dynamics of the Middle Atmosphere,* J. R. Holton and T. Matsuno, Eds., Terra, 3–18.

Pfister, L., S. Scott, and M. Loewenstein, 1993: Mesoscale disturbances in the tropical stratosphere excited by convection: Observations and effects on the stratospheric momentum budget. *J. Atmos. Sci.,* **50,** 1058–1075.

Pierrehumbert, R. T., 1986: An essay on the parameterization of orographic gravity wave drag. *Proc. Seminar/Workshop on Observation, Theory and Modeling of Orographic Effects, Vol. 1,* Shinfield Park, Reading, United Kingdom, ECMWF, 251–282.

Rind, D., R. Suozzo, N. K. Balachandran, A. Lacis, and G. Russel, 1988a: The GISS global climate–middle atmosphere model. Part I: Model structure and climatology. *J. Atmos. Sci.,* **45,** 329–370.

——, ——, and ——, 1988b: The GISS global climate–middle atmosphere model. Part II: Model variability due to interaction between planetary waves, the mean circulation and gravity wave drag. *J. Atmos. Sci.,* **45,** 371–386.

Sato, K., and T. J. Dunkerton, 1997: Estimates of momentum flux associated with equatorial Kelvin and gravity waves. *J. Geophys. Res.,* **102,** 26 247–26 261.

Smith, R. B., and Y.-L. Lin, 1982: The addition of heat to a stratified airstream with application to the dynamics of orographic rain. *Quart. J. Roy. Meteor. Soc.,* **108,** 353–378.